communications earth & environment

Article

https://doi.org/10.1038/s43247-024-01525-1

Local feedback and ENSO govern decadal changes in variability and seasonal synchronization of the Indian Ocean Dipole

Check for updates

Hyo-Jin Park [1], Soon-Il An [1,2,3] ✉, Jae-Heung Park [4], Malte F. Stuecker [5], Chao Liu [2] & Sang-Wook Yeh [6]

The Indian Ocean Dipole (IOD), characterized by an interannual fluctuation in zonal dipole pattern of sea surface temperature anomalies along the tropical Indian Ocean, has a large socioeconomic impact on neighboring countries. Here, we investigate the decadal modulations of IOD variability over the last 123 years (1900–2022), by analyzing the observational reanalysis data in conjunction with a low-order IOD model that accounts for both stochastic forcing and the remote impact of ENSO. The observed decadal changes in IOD variability are primarily attributed to the local air–sea coupled feedback, and secondarily to ENSO. The local feedback during the late winter has intensified since the late-1970s due to the Indian Ocean warming, the suppressed westerly winter monsoon in the southeastern Indian Ocean, the shallowing of the mean thermocline in the southeastern Indian Ocean, and the decrease in mean upwelling in the western Indian Ocean. Each of these enhances the convective instability, anomalous evaporative cooling, and oceanic vertical thermal advections, respectively. Intensified local feedback increases the likelihood of the early onset of IOD events in the late winter. Additionally, ENSO, which has strengthened since the mid-twentieth century, has extended the peak phase of IOD into the late fall in recent decades.

The Indian Ocean Dipole (IOD) is a primary interannual climate variability mode in the tropical Indian Ocean, which has a peak phase during the fall season (for convenience, the seasons in this study follow those in the Northern Hemisphere)[1–4]. During the positive phase, the southeastern tropical Indian Ocean sea surface temperature (SST) becomes colder, whereas the western tropical Indian Ocean SST becomes warmer than normal. The opposite pattern is observed during the negative phase[5–11]. Due to substantial climate impact of the IOD not only in neighboring countries but also in remote regions[5–9], an in-depth understanding of IOD dynamics is crucial for precise long-term climate prediction and the effective mitigation of climate risks associated with IOD events.

Despite its complexity, the development mechanism of the IOD can be largely understood by categorizing its contributors into three parts: the internal feedback process, external forcing, and stochastic forcing. Internal feedback processes include Bjerknes feedback (involving winds, thermocline tilt, and SST)[1,12], wind–evaporation–SST feedback[13], and cloud–radiation–SST feedback[14,15], which directly contribute to IOD development. In addition to the internal feedback process, the IOD is influenced by outside of the tropical Indian Ocean, such as the El Niño–Southern Oscillation (ENSO), subtropical IOD[16], and the North Tropical Atlantic[17]. Among them, ENSO is known to be the most influential on the IOD, as it not only initiates the IOD but also influences both its amplitude and spatiotemporal characteristics[4,15,18,19]. Likewise, stochastic forcing associated with the Madden–Julian Oscillation and weather noise can also independently initiate IOD events and modify IOD growth[19–22].

[1]Department of Atmospheric Sciences, Yonsei University, Seodaemun-gu, Seoul, Republic of Korea. [2]Irreversible Climate Change Research Center, Yonsei University, Seodaemun-gu, Seoul, Republic of Korea. [3]Division of Environmental Science and Engineering, Pohang University of Science and Technology, Pohang, Republic of Korea. [4]School of Earth and Environmental Sciences, Seoul National University, Seoul, Republic of Korea. [5]Department of Oceanography and International Pacific Research Center, School of Ocean and Earth Science and Technology, University of Hawai'i at Mānoa, Honolulu, HI, USA. [6]Department of Marine Science and Convergence Engineering, Hanyang University, ERICA, Ansan, Republic of Korea. ✉e-mail: sian@yonsei.ac.kr

Previous studies have shown that there has been a decadal-to-interdecadal modulation of the IOD variability during the last century by analyzing observational reanalysis datasets[23–26] and coral oxygen isotope records[27]. For example, negative IOD events with La Niña dominated prior to 1920s, and some weak positive events occurred independently of El Niño during 1920s–1950s, whereas strong and frequent positive IOD events associated with El Niño prevailed after 1950s[24,26]. Abram et al.[27] also showed an increasing trend in the frequency and strength of IOD events during the 20th century by analyzing coral oxygen isotope records. In particular, the frequent positive IOD events in recent decades have been suggested to be related to a gradual strengthening of the mean zonal SST (west-east) gradient (a positive IOD-like pattern), which drives anomalous easterly winds[28–30].

Likewise, IOD variability, the temporal evolution of the IOD has also been modulated on decadal timescales. Different from that typical IOD events have a peak phase in fall, early developed IOD events, which peak in summer, have been observed since the mid-1970s[31,32]. A previous study[32] argued that the frequent occurrence of early developed IOD events is related to the intensified Bjerknes feedback due to the weakening of the Walker circulation associated with positive IOD-like warming since the mid-1970s and the early onset of the summer monsoon.

Although previous studies have extensively investigated variations in IOD properties and their relationships with ENSO, an understanding of the observational decadal modulations of IOD variability and seasonal synchronization is still lacking, particularly from the perspectives of both internal processes and external forcings. Here, we quantitatively examine the extent to which specific processes contribute to the decadal modulation of the IOD, with particular emphasis on recent decades. To this end, the relative roles of internal and external factors are quantified over the past 123 years (1900–2022) of observational and reanalysis data, using a low-order IOD model. Through a line of investigation, we demonstrate that internal process is most prominent factor for the decadal modulation of IOD. Furthermore, while both internal process and ENSO forcing contribute to the recent increase in IOD variability, the internal process plays a critical role in occurrence of early developing IOD events.

Results

Decadal modulation of observed IOD variability

To examine decadal variation in the IOD, the 30-year moving variance of the 3-month to 8-year bandpass-filtered Dipole Mode Index (DMI) was computed (Fig. 1a; see Methods). Abrupt intensification of the IOD variability was first observed after the mid-1940s and then again after the late-1970s. The maximum IOD variance during the 2000s was more than double the minimum IOD variance around the 1940s, indicating substantial decadal modulation of IOD variance. Although the absolute value of the IOD variance of each reanalysis dataset was somewhat different, the overall tendency of the interdecadal variation of the IOD variance was similar among the eight reanalysis datasets (Supplementary Fig. 1). Therefore, the results of this study are not dependent on the selected dataset.

To analyze decadal modulation in the temporal evolution of the IOD, the 30-year moving variance of the DMI for each calendar month was computed, and the month with the maximum DMI variance was identified (Fig. 1b). Month with the strongest IOD variance is mostly observed in September, indicating a seasonal phase locking. Moreover, there are decadal fluctuations in a phase locking feature. The month with the strongest IOD variance was observed in August in the 1940s and in October in 1980s to 2000. Besides the peak phase change, the IOD variance in spring and summer has increased since the late-1970s (Supplementary Fig. 2a). This means that the variability of the IOD has been strengthened not only during fall season when IOD variability is strongest but also during spring to summer when IOD develops in recent decades, probably reflecting recent increased frequency of early developed IOD events[32].

Decadal changes in parameters of the IOD model

To reveal the origins of the decadal modulation of IOD properties, we adopted a low-order IOD model, including parameters such as growth rate (λ_m; a damping rate with an opposite sign), ENSO forcing (β_m), and noise residual (σ_m) (please refer to the Method). Subsequently, we computed the parameters of the IOD model with a 30-year moving window, where the window was moved by one-year. To validating the performance of the model, we reconstructed the DMI using the IOD model in each window, where integration was performed with the real initial condition and repeated 1000 times by inputting another random noise. By doing so, we reproduced a 30-year moving variance time series by concatenating the averages of the variances calculated for each of the 1000 noise ensembles.

The correlation coefficient between the observed and reproduced 30-year moving DMI variance was 0.95, which was statistically significant at a 99% confidence level by Student's *t*-test with an effective degree of freedom (DOF) of 5.9, wherein the root mean squared error (RMSE) was 0.09 (Fig. 1a). Moreover, the 30-year moving variance of the reconstructed DMI for each calendar month was similar to that of the original data with

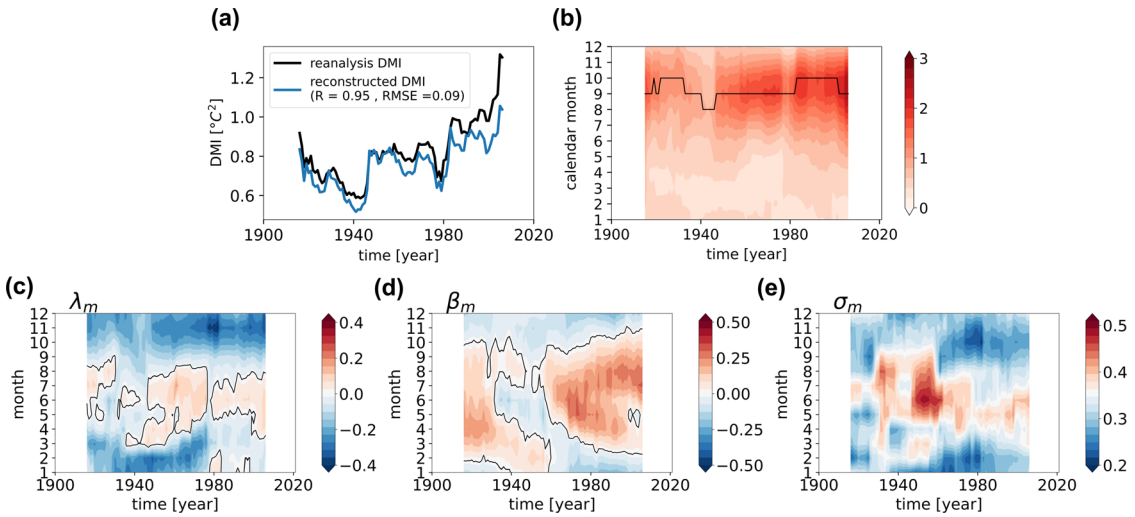


Fig. 1 | Decadal changes in IOD variability and parameters of the IOD model. **a** Timeseries of the centered 30-year moving variance [°C^2] of the reanalysis DMI (black line) and the reconstructed DMI variance by using the IOD model (blue line) during 1900–2022. **b** The 30-year moving variance of the band-pass filtered and normalized DMI for each calendar month (shading). The peak month has a 30-year moving DMI variance and each year is indicated by the black curve. 30-year monthly moving timeseries of (**c**) damping rate λ_m [month^{-1}], (**d**) ENSO-forcing parameter β_m [month^{-1}], and (**e**) noise standard deviation σ_m [°C month^{-1}] for the IOD model. The black contour lines are the zero contours.

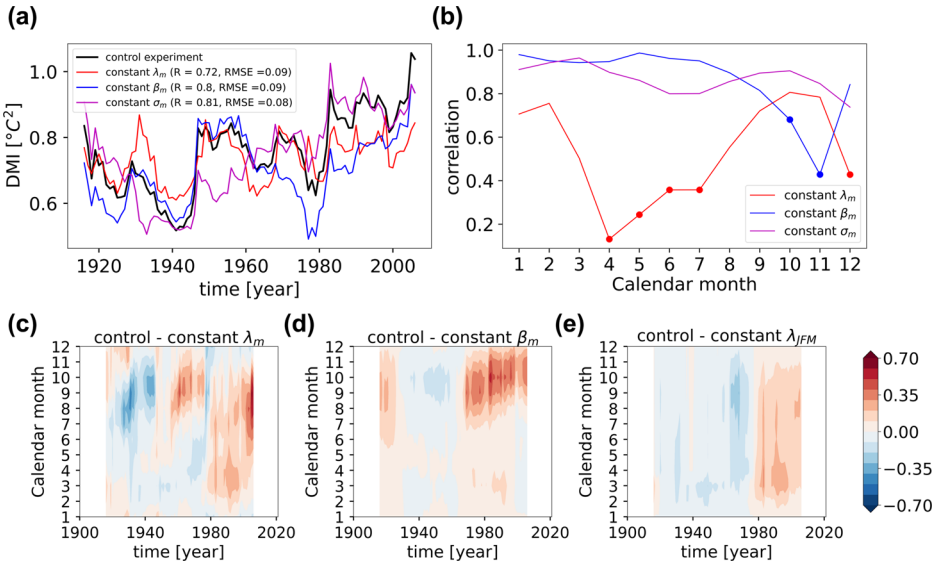


Fig. 2 | Each role of IOD model parameters in decadal changes of IOD variability. **a** The timeseries of centered 30-year moving variance of the reconstructed DMI obtained from the IOD model for the control experiment (black line; [°C^2]), and one parameter experiment (colored lines; [°C^2]). In control experiment, all parameters are time varying. In one parameter experiment, one of the three parameters (λ_m(red line), β_m (blue line), and σ_m (purple line)) is kept a constant of its climatological-mean value. The correlation and RMSE between the 30-year moving DMI variance for the different reconstructions are shown as inserts. **b** Correlation coefficient for each calendar month in 30-year moving DMI variances between the control experiment and each constant parameter experiment. The dots in Fig. 2b indicate insignificant correlations at the 95% confidence level using a Student's t test, and otherwise statistically significant. The effective degrees of freedom are calculated by each calendar month. **c**–**e** Shows the differences in 30-year moving monthly variances [°C^2] between the control experiment and each constant parameter experiment for (**c**) λ_m, (**d**) β_m, and (**e**) λ_{JFM}.

statistical significance (Supplementary Fig. 3). Therefore, we conclude that the IOD model is suitable for investigating the decadal variations of the IOD variance on monthly timescales, despite some biases which arise from unconsidered factors in the IOD model, such as the influence of the Atlantic Ocean or subtropical oceans, as well as nonlinear processes[22].

Strong decadal changes in each parameter are shown in Fig. 1c–e. For ease of interpretation, the original value was subtracted from climatology to assess the extent of the increase or decrease (Supplementary Fig. 2). The growth rate λ_m during summer reached a minimum around the 1940s and a maximum around the 1960s, increasing by approximately 110% compared to the 1940s. Meanwhile, λ_m in January-February-March (JFM), when the IOD damps, shows a pronounced increase since the late-1970s by about 113% and even positive values for some decades (Fig. 1c). Comprehensively, the minimum λ_m in JJA in the 1940s and the pronounced increase of the λ_m in JFM after the late-1970s correspond to the weak IOD amplitude in the 1940s and the strong increasing trend of the IOD amplitude since the late-1970s, respectively (Fig. 1a).

The ENSO parameter (β_m) showed an annual cycle with a peak in April before the 1940s, and then its overall amplitude tends to decrease until 1960s. Afterwards, the amplitude of β_m is recovered. Interestingly, its peak moved from May to July between 1960s and 1980s as widening (Fig. 1d). That is, duration in which ENSO influences the IOD has been increased in the late twentieth century. However, unlike the significant relationship between growth rate λ_m and DMI variance (correlation coefficient of 0.77 with DOF = 10.4, 99% confidence level), the relationship between ENSO parameter (β_m) and the DMI variance is insignificant (correlation coefficient of 0.38 with DOF = 5.7) on a yearly timescale.

On the other hand, the noise residual (σ_m), reflecting weather noise or other missing physics, also shows an annual cycle with a peak in June, especially between the 1950s and 1960s, probably related to the abrupt increase in DMI variability during that period (Fig. 1e).

Decadal changes in IOD variability

To quantify the factors responsible for the decadal changes in IOD variability, we performed sensitivity experiment using the IOD model. In this experiment, one of the three parameters (λ_m, β_m, and σ_m) was held constant at its climatological mean value (1900–2022), while the other two parameters were varied. When the growth rate (λ_m) is maintained at its climatological mean, the correlation coefficient between the resulting 30-year moving DMI variance and the control experiment (i.e., all three parameters are time-varying) is 0.72 (DOF = 15.5, p-value = 0.002, RMS = 0.09). Likewise, when the ENSO parameter (β_m) is held constant or when the noise forcing (σ_m) does, the corresponding correlation coefficients are 0.80 (DOF = 7.6, p-value = 0.02, RMS = 0.09) and 0.81 (DOF = 6.6, p-value = 0.04, RMS = 0.08), respectively. Hence, the primary factor responsible for the decadal modulations in IOD variability is identified as changes in the growth rate (λ_m), with changes in the ENSO (β_m) and noise (σ_m) playing secondary roles (Fig. 2a).

To assess when and to what extent changes in each parameter influenced IOD variance, we examined the difference in DMI variances and the correlation between the control and sensitivity experiments by fixing a parameter (constant-parameter) (Fig. 2b–e). The correlation analysis between the control experiment and the constant-parameter experiment shows a statistically significant reduction from April to July when growth rate (λ_m) kept constant, whereas when ENSO parameter (β_m) is fixed, the reduction of correlation is evident in October and November (Fig. 2b). This implies that temporal changes in the ENSO impact are a dominant factor influencing IOD variance in fall season. On the other hand, the time-varying growth rate (λ_m) acts to enhance IOD variance from spring to summer after the late-1970s (Fig. 2c). This effect becomes even stronger after the 2000s. The time-varying ENSO parameter (β_m) causes the increased variance since the late-1960s, especially fall season (Fig. 2d). In comparison, the impact of noise (σ_m) is not as remarkable as that of growth rate (λ_m) and ENSO (β_m) (Fig. 2b).

To quantify the relative role of each factor leading to the abrupt increase in DMI variance since the late-1970s, we compare DMI variance difference between before and after 1980 (1953–1978 (P1) versus 1980–2005 (P2)) of two experiments (constant either λ_m or β_m). Note that noise (σ_m) is not associated with the abrupt increase after 1980. In the control experiment, the DMI variance increased by approximately 16% in P2 compared to

Table 1 | Contribution of λ_m and β_m to the increase in IOD variance after 1980

Experiment	control	constant λ_m	constant β_m
Before 1980 (P1)	0.76	0.73	0.70
After 1980 (P2)	0.89	0.78	0.77
After-Before (%)	0.12 (16%)	0.05 (7%)	0.07 (10%)

DMI variance before 1980 (P1) and after 1980 (P2) in each experiment (control, constant λ_m, and constant β_m) and the difference between two periods.

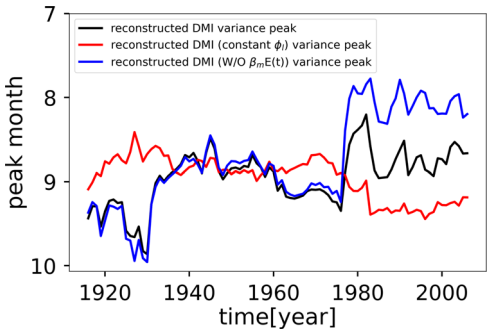


Fig. 3 | Each role of IOD model parameters in decadal changes of IOD seasonal synchronization. Timeseries of DMI peak month obtained from the control experiment (black line), the constant φ_l experiment (red line), and the non-ENSO-forcing experiment ($\beta_m E(t)$; blue line). DMI peak month is determined over 30-year moving band by computing DMI variance for each calendar month for each band.

P1 (Table 1). However, the constant $\lambda_m$experiment captured only 7% of the abrupt increase in IOD variance. While in the constant β_m experiment, DMI variance increased by 10%, capturing more than half the increase in the control experiment. Therefore, the observed abrupt increase in IOD variance since the late-1970s was due to both an increased growth rate (λ_m) and a strengthened ENSO effect (β_m).

IOD seasonal synchronization

In the previous section, we demonstrated that both the growth rate (λ_m) and the ENSO forcing (β_m) have a dominate annual cycle. Consequently, our objective is to comprehend the temporal evolution of IOD and its decadal change, in association with their annual cycles. Here, we quantified the respective roles of the IOD growth rate and ENSO effect on decadal changes in IOD seasonal synchronization using the IOD model. As a first step, the growth rate (λ_m) is approximated using a sinusoid[19]:

$$\lambda_m \approx \lambda_0 + \lambda_a \cos(\omega_a t + \varphi_l) \quad (1)$$

where φ_l is the phase of the annual cycle and $\omega_a = \frac{2\pi}{12}[month^{-1}]$ is the angular frequency of the annual cycle. Thus, growth rate (λ_m) is linearly separated into annual mean (λ_0) and annual cycle parts ($\lambda_a \cos(\omega_a t + \varphi_l)$). We note that the decadal changes in the peak phase of DMI variance with modulated growth rate above were almost identical to those observed (Supplementary Fig. 4). Subsequently, two additional sensitivity experiments are conducted. In the first experiment, we removed the ENSO forcing term ($\beta_m E(t)$) to explore its role, in which all other parameters remained time-varying, as in the control experiment. In the second experiment, meanwhile the phase of growth rate ($\lambda_m(\varphi_l)$) was fixed as its climatological value (1900–2022) to explore its role. This is because the IOD model does not properly reproduce the DMI without the growth rate term.

When ENSO forcing ($\beta_m E(t)$) is set to zero in the IOD model, the peak phase of DMI variance in calendar months is shifted forward by 0.9 months since the late-1970s (Fig. 3). In contrast, when φ_l is fixed as a climatology for whole period, the peak timing of the reconstructed DMI variance remains unchanged until 1980s, and it is slightly delayed thereafter (Fig. 3). In other words, IOD events influenced by the ENSO reached their peak phases at a later time, whereas those independent of the ENSO attained their peak phases earlier. Therefore, our results suggest that an enhanced growth rate in winter resulted in earlier IOD growth, whereas the ENSO led to a delay in IOD growth after 1980s.

Rapid growth of IOD starting from winter season

In the previous section, we showed that an enhanced growth rate (λ_m) is the main cause for the abrupt increase in IOD variance since the late-1970s, particularly in JFM (Figs. 1c, 2c). To further verify this finding, we divided the calendar year into four seasons, ranging from JFM to October–November–December (OND), and conducted additional sensitivity experiments. In these experiments, we maintained the growth rate (λ_m) for one specific season at its climatological-mean value (from 1900 to 2022), while allowing the growth rate for all other seasons to vary over time. All other parameters except λ_m were varying over time as in the control experiment. When the growth rate in JFM (λ_{JFM}) was kept constant at its climatological value, the IOD variance exhibited an increase during P1 period (1953–1978) and a decrease during P2 period (1980–2005) in all calendar months (Fig. 2e). It indicates that the decadal changes in λ_{JFM} are significant modulating IOD variance. On the other hands, when the growth rate was allowed to vary in each of the other seasons, only minor or opposite decadal changes in DMI variance were observed (Supplementary Fig. 5). A exception to this trend is noted in the growth rate in April-May-June season (AMJ), which has significantly contributed to an increase in IOD variance, but only since the 2000s (Supplementary Fig. 5). In summary, we confirm that the early IOD growth during the winter season plays a crucial role in the notable increase in IOD variance observed between P1 and P2 periods.

To get a better dynamical insight on the rapid growth of IOD events, especially in relation to the enhanced local feedback (i.e., λ_m) since the late-1970s, we analyzed the regression patterns of various physical variables associated with the IOD. We focused on comparing two distinct periods: 1953–1978 (P1) and 1980–2005 (P2) (Supplementary Fig. 6), in terms of the growing tendency of IOD during JFM, which was estimated by computing the difference in the regression pattern against the September–October–November (SON) DMI between April and January, using the forward Euler discretization method. The growing tendencies of tropical Indian Ocean SST, sea-level pressure (SLP), wind stress, and subsurface temperature anomalies with respect to the following autumn (SON) normalized DMI were calculated for each P1 and P2 periods, and their differences (P2–P1) (Fig. 4). In P1 period, the growing tendency pattern in SST resembled a negative IOD – like pattern, suggesting the limited IOD development (Fig. 4a). Conversely, in P2 period, a positive IOD – like pattern, inferring early development of IOD, was observed, characterized by warming in western IO and cooling in eastern IO, along with high SLP anomalies (gray contours) extending further westward and anomalous southeasterly winds (Fig. 4b). The emergence of anomalous SLP high associated with these anomalous southeasterly winds seems to linked to the subtropical IOD during the winter season (Fig. 4b), aligning with previous studies that have noted an increased connection between the IOD and the subtropical Indian Ocean since the late-twentieth century[16,33]. The difference in the growing tendency between P1 and P2 clearly demonstrates the enhanced IOD growth during the winter season (Fig. 4c).

The IOD-related oceanic subsurface change also supports stronger IOD growing tendency in JFM. In P1 period, there was a weak subsurface cooling tendency observed in both the eastern and western IO (Fig. 4a). However, during P2 period, the strong subsurface warming in western IO and cooling in southeastern IO, along with easterly anomalies in surface winds were observed. This pattern resembles the anomalous subsurface temperature pattern observed during the positive IOD events, suggesting a significant increase in the growing tendency of IOD (Fig. 4b). Moreover, the zonal contrasting pattern in the growing tendency of sea surface height anomalies during P2 period is more pronounced compared to P1 period, consistently indicating the enhanced early growth of IOD during P2 period

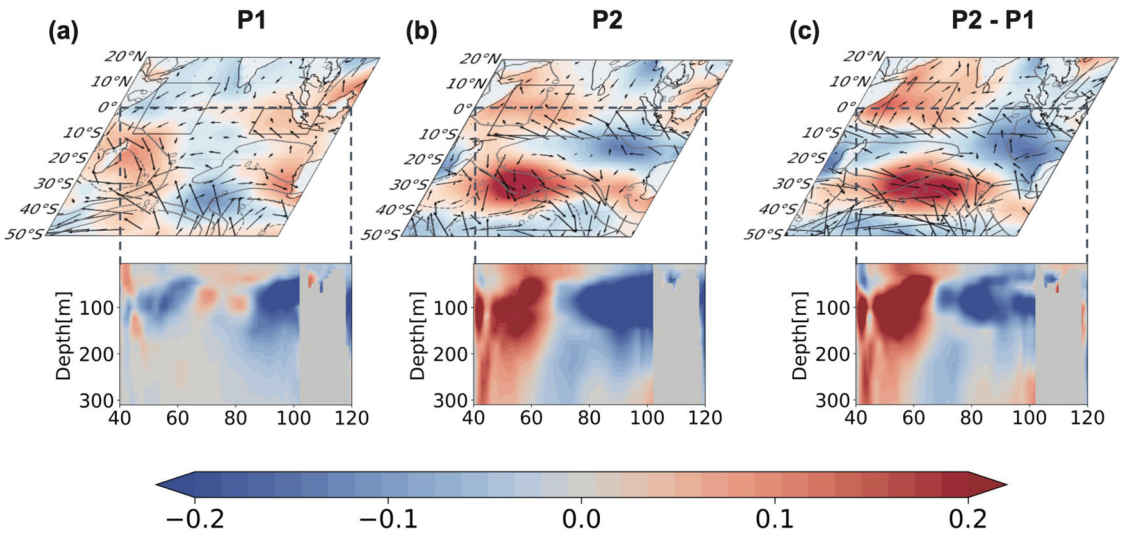


Fig. 4 | Winter mean changes associated with IOD variability for two decadal periods. a Difference between April and January regression map of SST (shading, [°C]), wind stress (vector, [N m^{-2}]), sea level pressure anomalies (gray contours, 0.3 [hPa]), and subsurface temperature (5°S to 5°N) anomaly (shading, [°C]) against the September–October–November mean normalized DMI during P1 (1953–1978). (**b**) same as in (**a**) but for P2 (1980–2005). (**c**) difference between (**b**) and (**a**). Boxes in figure indicate the western and eastern pole of IOD.

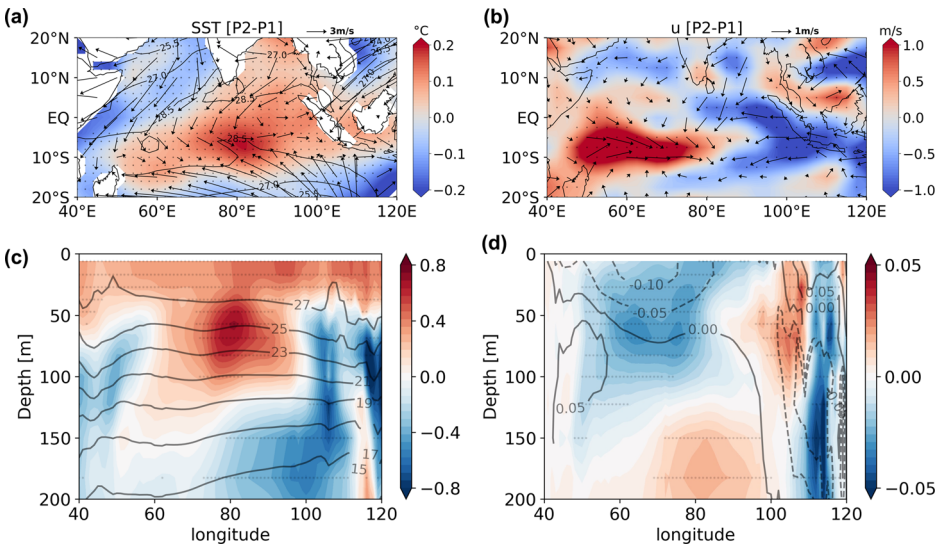


Fig. 5 | Observed winter climatological mean changes over 1948–2022. a Climatological January-February-March (JFM) mean SST (contours) and surface winds (vectors) for whole available data periods (1948–2022), and differences in JFM-mean SST (color shading) between P1 and P2 periods (Unit: °C). **b** As in (**a**) except for climatological JFM-mean surface zonal winds (color shading) and differences in surface winds (vectors) (unit: ms^{-1}). **c** As in (**a**) except for the longitude-depth section of the climatological JFM mean ocean subsurface temperature averaged over 10°S–5°N (contour) and differences in ocean subsurface temperature (color shading). **d** As in (**c**) expect for the zonal ocean current averaged over 10°S–5°N (unit; ms^{-1}). In case of SST, area-averaged difference of SST over Indian Ocean domain (20°S–20°N, 40°E –100°E) has been removed. Stippling area by black dots indicate statistically significant values at the 95% confidence level, determined by a Student's t-test with n−2 degrees of freedom.

(Supplementary Fig. 7). Consequently, the increase in growing tendency of IOD during winter is evident not only at the surface but also in the subsurface ocean.

Mean state changes contributing to the rapid growth of IOD during winter

In previous section, we demonstrated that the increased growth rate in the late winter was a key factor in the recent decadal changes in IOD variability. Here, we investigate how the changes in the climatological mean state intensify the air-sea coupled feedback, which is linked to the early emergence of IOD during the winter season. In the following, we qualitatively assess the influence of the climate state changes, specifically between P1 and P2 periods, on air-sea coupled feedback, considering both thermodynamic and dynamic aspects.

The climatological mean SST in the tropical IO during the boreal winter season typically exceeds 28 °C (Fig. 5a), a threshold sufficient to induce convective instability. During the P2 period, the SST is observed to be higher in most areas of the tropical IO compared to the P1 period. As a result, the response of atmospheric convection, along with its corresponding variability to SST changes, is expected to be more pronounced, leading to an enhancement in air-sea coupling during P2 period. Additionally, there is a noticeable weakening of the westerly winter monsoon flow over the southeastern IO during P2 period, particularly off the coast of Sumatra (Fig. 5a, b). Typically, from a wind-evaporation-SST (WES) feedback perspective, when easterly (westerly) anomalies occur, the decrease (increase) in mean wind speed leads to reduced (increased) evaporation, resulting in anomalous warming (cooling) of SST. This implies that the feedback acts as a hindering factor in the development of the IOD. However, as the mean westerly weakens and occasionally shifts to easterlies (P2), it becomes an ineffective suppressing mechanism and may instead contribute to the growth of IOD during the winter season (Supplementary Fig. 8).

The weakening of the northwesterly winter monsoon flow over the southeastern IO (Fig. 5b) leads to the shoaling of thermocline near off the coast of Sumatra (between 100° and 120°E; Fig. 5c). Moreover, changes in

sea surface height (SSH) are consistent with thermocline shoaling during P2 period such that SSH in the IOD-eastern region significantly decreased (Supplementary Fig. 9), with a 99% confidence level, from 47.5 cm to 45.8 cm (p-value < 0.001). The shallower mean thermocline observed during P2 period leads to the enhancement in coupling feedback between the atmosphere and ocean[34,35]. by increasing the sensitivity of the mixed layer temperature to change in anomalous thermocline depth in southeastern IO during P2 period compared to P1 period. Such enhanced sensitivity contributes to a stronger interaction and feedback mechanism between the ocean and atmosphere in the IOD region.

The climatological westward surface current on the equatorial region (5°S–5°N and 40–80°E) during the late winter season is a significantly strengthened from $-0.06\,ms^{-1}$ in P1 to $-0.08\,ms^{-1}$ in P2 with a 99% confidence (Fig. 5d). This change is presumably driven by the strengthened easterly wind in the central equatorial Indian Ocean region (3°S–3°N and 70–85°E) (from $-0.0005\ Nm^{-2}$ to $-0.003\,Nm^{-2}$, p-value < 0.1). This strengthened easterly wind and the westward mean current in the equatorial IO is dynamically linked to the significant decrease in mean upwelling in the IOD-western region (from $0.1\,m\ month^{-1}$ to $-0.5\,m\ month^{-1}$, p-value = 0.0002).

In summary, from a thermodynamical perspective, the rise in mean SST in the tropical IO coupled with the weakening of the westerly winter monsoon flow over the southeastern IO contributes to an intensification of air-sea coupling strength. On the dynamical front, the reduction in mean upwelling in the western IO and the shallowing of the mean thermocline in the southeastern IO enhance the air-sea coupling feedback through the intensification of the thermocline feedback mechanism. Consequently, these changes in the climatological mean state during the P2 Period result in a strengthened growth rate of the IOD during the boreal winter season. These combined thermodynamic and dynamic changes effectively contribute to the observed increase in the IOD's intensity and variability during this period.

Discussion

Over the last 123 years, the variability of IOD has undergone two abrupt and stepwise increases: the first in the mid-1940s and the second in the late-1970s. This study aimed to unveil the physical mechanisms behind the decadal modulation of the IOD variance, utilizing reanalysis data and a low-order IOD model. The low-order IOD model well reproduced the observed decadal changes in the IOD variance, including its peak timing within the seasonal cycle and its changes.

Firstly, we found that the decadal change in the IOD growth rate (or the local feedback strength of the IOD) is the primary factor for the decadal variation in IOD variance, and ENSO plays a secondary role. Since the late-1970s, there has been a notable strengthening of the IOD growth rate, especially from the late winter to early spring, which significantly affects IOD development from spring to summer. The influence of ENSO on the IOD, which intensified since the 1960s, extended the IOD growth period from the 1980s onward (Fig. 3). This altered ENSO effect corresponds with both an increase in ENSO variance (by about 10% in P2 period compared to P1 period) and the ENSO-IOD connection (Supplementary Fig. 10a, b, respectively). The increased ENSO variance during P2 period is responsible for the overall increase in the DMI variance (Supplementary Fig. 10a). Moreover, the correlations between monthly DMI and Niño3.4 on September through December during P2 period are significantly stronger than those during P1 period, indicating a significant contribution to increase DMI variance, especially during the fall to early winter season (Supplementary Fig. 10b).

Secondly, we found that while the IOD growth rate remains the dominant factor in determining IOD seasonal synchronization, the influence of the ENSO forcing has become more dominant in recent decades. These two factors had opposite effects on IOD seasonal synchronization in the late 20th century such that the seasonal phase of the IOD damping rate advanced by ~0.9 month, while the ENSO effect was delayed by ~0.4 month. This result explains the more frequent occurrence of early IOD events, apart from ENSO, in recent decades.

Lastly, our study demonstrates that the rapid increase in the growth rate of IOD during JFM season is the primary contributor to the increase in IOD variance since the late 1970s. This marked rise in the IOD's growth rate during the JFM season can be ascribed to several key factors occurring in the recent decades: the overall surface warming across the tropical Indian Ocean (IO), the weakening of the westerly winter monsoon flow in the southeastern IO, the shallowing of the mean thermocline in the southeastern IO, and the decrease in mean upwelling in the western IO. These decadal changes have served to amplify the air-sea coupling process in each of these specific areas during the recent decadal periods. This enhanced coupling has, in turn, played a significant role in driving the observed changes in the behavior and intensity of the IOD, particularly in its growth rate during the JFM season.

The low-order IOD model utilized in this study is based on a linear system, which tends to underestimate the amplitude of extreme IOD events, such as those that occurred in 1997, 2016, and 2019. Additionally, the IOD model did not account for the spatial diversity of ENSO, as it solely relied on Niño3.4 index to represent ENSO forcing. For example, there has been an increased frequency of central Pacific El Niño events since the early 1990s[36–39], which may influence the IOD differently compared to the conventional ENSO events[40]. Despite these limitations, the IOD model well reproduced an increase in the IOD variance observed in recent decades. Furthermore, the linear framework allowed us to delineate the relative role of each process in contributing to the IOD variance changes over time. The current state-of-the-art climate models exhibit considerable uncertainty in their future projections of IOD variability in warmer climates[28,29]. While some models projected increased IOD variability, others do not. Therefore, there is an urgent need to better understand how changes in the mean climate state and other climate phenomena influence the IOD. In this study, by analyzing IOD variability over the last century, we quantified the processes driving these variations in IOD variance over the historical period. Applying our framework to longer observational records and future projections will help reduce some of these uncertainties.

Methods

Datasets

The primary dataset used in this study was the Extended Reconstructed Sea Surface Temperature version 5 (ERSST v5)[41] from 1900 to 2022 with a horizontal resolution of 2° × 2°. We also examined IOD decadal variability modulation using different observational and reanalysis products for their respective available time periods. These datasets include the Hadley Center Global Sea Ice and Sea Surface Temperature version 1.1 (HadISST)[42], Centennial in Situ Observation Based Estimates of SST (COBE)[43], NOAA Optimum Interpolation SST version 2[44], European Center for Medium-Range Weather Forecasts Ocean Reanalysis System 5[45], Simple Ocean Data Assimilation version 2.2.4 (SODA2.2.4)[46], and National Centers for Environmental Prediction Global Ocean Data Assimilation System (GODAS)[47] and the German contribution to the Estimating the Circulation and Climate of the Ocean project, version 3 (GECCO3)[48]. For SODA2.2.4, GODAS, and GECCO3, a potential temperature of 5 m was used to represent the SST. To further investigate the reasons behind decadal changes in IOD growth, we analyzed SLP, u, and v data for 1948–2018 obtained from the National Centers for Environmental Prediction/National Center for Atmospheric Research (NCEP/NCAR)[49] reanalysis. We also analyzed HadISST and slp data from the Met Office Hadley Centre (HadSLP2)[50], which yielded similar results. wherein the analysis period was from 1948 to 2018.

Indices

To investigate the interannual variability of the IOD, a bandpass filter (3-month to 8-year) was applied to the quadratic detrended SST. The results of this study are not sensitive to the detrending method. The IOD is defined as the difference in SST anomalies between the western TIO (50°E to 70°E and

10°S to 10°N) and southeastern TIO (90°E to 110°E and 10°S to the equator) and is known as the Dipole Mode Index (DMI)[1]. To describe ENSO, the Niño3.4 index was adopted, which indicates the average SSTA over the tropical Pacific Ocean (170°W to 120°W and 5°S to 5°N). All indices were normalized prior to the analysis.

A low-order IOD model

To investigate the decadal change in the IOD, we used a low-order stochastic-deterministic model (hereafter IOD model[19,21,22,51,52]) as follows:

$$\frac{\partial T}{\partial t} = \lambda_m T(t) + \beta_m E(t) + \sigma_m \xi_t \quad (2)$$

where T is the DMI, $E(t)$ is the Niño3.4 index, and ξ_t is Gaussian white noise with zero mean and unit standard deviation. The subscript 'm' indicates the calendar month (m = 1, 2, …,12). The parameters λ_m, β_m and σ_m are measures of the damping rate determined by local IO feedback processes, the sensitivity parameter of DMI to the external ENSO forcing, and the amplitude of the stochastic forcing, respectively. A least-square fitting with the forward Euler method was applied to the band-pass filtered and normalized DMI and Niño3.4 indices to compute λ_m and β_m for each calendar month. Then, σ_m is calculated as the standard deviation of the residual for each calendar month. The autocorrelation of the residuals was close to that of white noise, indicating that the stochastic forcing term in the IOD model refers to a random process. Using the estimated parameters, a reconstructed DMI was calculated at one-month time steps by integrating the model forward.

First, we calculated each parameter using all 123 years of the three datasets (ERSSTv5, HadISST, and COBE) to examine the general characteristics of the parameters. All three parameters showed an annual cycle (Supplementary Fig. 11)[22] The damping rate λ_m shows a maximum in the summer and strong decrease after fall. The remote impact of ENSO β_m is positive throughout most of the year except during winter. This positive impact reflects the characteristic of the IOD growing simultaneously with ENSO from spring to fall. The noise residual σ_m is always positive and reaches its maximum in June, coinciding with the timing of the active stochastic forcing responsibility for initiating IOD events. In summary, the seasonal evolution of these three parameters provides an understanding of various seasonally varying IOD processes.

Data availability

ERSSTv5 is available from https://psl.noaa.gov/data/gridded/data.noaa.ersst.v5.html; the HadISST from https://www.metoffice.gov.uk/hadobs/ the COBE from https://psl.noaa.gov/data/gridded/data.cobe.html; the OISST https://psl.noaa.gov/data/gridded/data.noaa.oisst.v2.highres.html; the ORAS5 https://cds.climate.copernicus.eu/cdsapp#!/dataset/reanalysis-oras5?tab=form; the SODA http://apdrc.soest.hawaii.edu/datadoc/soda_2.2.4.php; the GODAS https://psl.noaa.gov/data/gridded/data.godas.html; the GECCO3 https://www.cen.uni-hamburg.de/en/icdc/data/ocean/reanalysis-ocean/gecco3.html; the NCEP/NCAR R1 https://psl.noaa.gov/data/gridded/data.ncep.reanalysis.html.

Code availability

Any codes used in the manuscript are available upon request from H.-J Park, hjpark1021@yonsei.ac.kr

Received: 16 January 2024; Accepted: 21 June 2024;
Published online: 29 June 2024

References

1. Saji, N., Goswami, B., Vinayachandran, P. & Yamagata, T. A dipole mode in the Tropical Ocean. *Nature* **401**, 360–363 (1999).
2. Webster, P. J., Moore, A. M., Loschnigg, J. P. & Leben, R. R. Coupled ocean-atmosphere dynamics in the Indian Ocean during 1997–98. *Nature* **401**, 356–360 (1999).
3. Annamalai, H. et al. Coupled dynamics over the Indian Ocean: spring initiation of the Zonal Mode. *Deep Sea Res. Part II: Topical Stud. Oceanogr.* **50**, 2305–2330 (2003).
4. An, S. I. A dynamic link between the basin-scale and zonal modes in the Tropical Indian Ocean. *Theor. Appl Climatol.* **78**, 203–215 (2004).
5. Ashok, K., Guan, Z. & Yamagata, T. Impact of the Indian Ocean dipole on the relationship between the Indian monsoon rainfall and ENSO. *Geophys Res Lett.* **28**, 4499–4502 (2001).
6. Black, E., Slingo, J. & Sperber, K. R. An observational study of the relationship between excessively strong short rains in coastal East Africa and Indian ocean SST. *Mon. Weather Rev.* **131**, 74–94 (2003).
7. Clark, C. O., Webster, P. J. & Cole, J. E. Interdecadal variability of the relationship between the Indian Ocean zonal mode and East African coastal rainfall anomalies. *J. Clim.* **16**, 548–554 (2003).
8. Zubair, L., Rao, S. A. & Yamagata, T. Modulation of Sri Lankan Maha rainfall by the Indian Ocean Dipole. *Geophys. Res. Lett.* **30**, 1063 (2003).
9. Saji, N. H. & Yamagata, T. Possible impacts of Indian Ocean Dipole mode events on global climate. *Clim. Res* **25**, 151–169 (2003).
10. Cai, W. et al. Increased frequency of extreme Indian ocean dipole events due to greenhouse warming. *Nature* **510**, 254–258 (2014).
11. Luo, J.-J. et al. Current status of intraseasonal–seasonal-to-interannual prediction of the indo-pacific climate. in 63–107 https://doi.org/10.1142/9789814696623_0003 (2022).
12. Bjerknes, J. Atmospheric teleconnections from the equatorial pacific. *Mon. Weather Rev.* **97**, 163–172 (1969).
13. Xie, S.-P. & Philander, S. G. H. A coupled ocean-atmosphere model of relevance to the ITCZ in the eastern Pacific. *Tellus, Ser. A* **46 A**, 340–350 (1994).
14. Li, T., Wang, B., Chang, C. P. & Zhang, Y. A theory for the Indian Ocean dipole-zonal mode. *J. Atmos. Sci.* **60**, 2119–2135 (2003).
15. Fischer, A. S., Terray, P., Guilyardi, E., Gualdi, S. & Delecluse, P. Two independent triggers for the Indian Ocean dipole/zonal mode in a coupled GCM. *J. Clim.* **18**, 3428–3449 (2005).
16. Zhang, L. Y. et al. Triggering the Indian Ocean Dipole From the Southern Hemisphere. *Geophys Res Lett.* **47**, 1–9 (2020).
17. Zhang, G., Wang, X., Xie, Q., Chen, J. & Chen, S. Strengthening impacts of spring sea surface temperature in the north tropical Atlantic on Indian Ocean dipole after the mid-1980s. *Clim. Dyn.* **59**, 185–200 (2022).
18. Yang, Y. et al. Seasonality and predictability of the Indian Ocean dipole mode: ENSO forcing and internal variability. *J. Clim.* **28**, 8021–8036 (2015).
19. Stuecker, M. F. et al. Revisiting ENSO/Indian Ocean Dipole phase relationships. *Geophys Res Lett.* **44**, 2481–2492 (2017).
20. McKenna, S. et al. Indian Ocean Dipole in CMIP5 and CMIP6: characteristics, biases, and links to ENSO. *Sci. Rep.* **10**, 11500 (2020).
21. An, S.-I. et al. Intensity changes of Indian Ocean dipole mode in a carbon dioxide removal scenario. *NPJ Clim. Atmos. Sci.* **5**, 20 (2022).
22. An, S.-I. et al. Main drivers of Indian Ocean Dipole asymmetry revealed by a simple IOD model. *NPJ Clim. Atmos. Sci.* **6**, 93 (2023).
23. Ashok, K., Chan, W.-L., Motoi, T. & Yamagata, T. Decadal variability of the Indian Ocean dipole. *Geophys. Res. Lett.* **31**, L24207 (2004).
24. Kripalani, R. H. & Kumar, P. Northeast monsoon rainfall variability over south peninsular India vis-à-vis the Indian Ocean dipole mode. *Int. J. Climatol.* **24**, 1267–1282 (2004).
25. Tozuka, T., Luo, J., Masson, S. & Yamagata, T. Decadal modulations of the Indian Ocean dipole in the SINTEX-F1 coupled GCM. *J. Clim.* **20**, 2881–2894 (2007).
26. Ihara, C., Kushnir, Y. & Cane, M. A. Warming Trend of the Indian Ocean SST and Indian Ocean Dipole from 1880 to 2004. *J. Clim.* **21**, 2035–2046 (2008).
27. Abram, N. J., Gagan, M. K., Cole, J. E., Hantoro, W. S. & Mudelsee, M. Recent intensification of tropical climate variability in the Indian Ocean. *Nat. Geosci.* **1**, 849–853 (2008).

28. Zheng, X.-T., Xie, S.-P., Vecchi, G. A., Liu, Q. & Hafner, J. Indian Ocean Dipole Response to Global Warming: Analysis of Ocean–Atmospheric Feedbacks in a Coupled Model. *J. Clim.* **23**, 1240–1253 (2010).
29. Cai, W. et al. Projected response of the Indian Ocean Dipole to greenhouse warming. *Nat. Geosci.* **6**, 999–1007 (2013).
30. Han, W. et al. Indian Ocean Decadal Variability: A Review. *Bull. Am. Meteorol. Soc.* **95**, 1679–1703 (2014).
31. Du, Y., Cai, W. & Wu, Y. A New Type of the Indian Ocean Dipole since the Mid-1970s. *J. Clim.* **26**, 959–972 (2013).
32. Sun, S., Fang, Y., Zu, Y., Liu, L. & Li, K. Increased occurrences of early Indian Ocean Dipole under global warming. *Sci. Adv.* **8**, eadd6025 (2023).
33. Anila, S. & Gnanaseelan, C. Coupled feedback between the tropics and subtropics of the Indian Ocean with emphasis on the coupled interaction between IOD and SIOD. *Global and Planetary Change* **223**, 104091 (2023).
34. Shi, J., Fedorov, A. V. & Hu, S. A Sea Surface Height Perspective on El Niño Diversity, Ocean Energetics, and Energy Damping Rates. *Geophys Res Lett.* **47**, e2019GL086742 (2020).
35. Rebert, J. P., Donguy, J. R., Eldin, G. & Wyrtki, K. Relations between sea level, thermocline depth, heat content, and dynamic height in the tropical Pacific Ocean. *J. Geophys Res Oceans* **90**, 11719–11725 (1985).
36. Ashok, K., Behera, S. K., Rao, S. A., Weng, H. & Yamagata, T. El Niño Modoki and its possible teleconnection. *J. Geophys. Res. Oceans* **112**, C11007 (2007).
37. Kao, H.-Y. & Yu, J.-Y. Contrasting Eastern-Pacific and Central-Pacific Types of ENSO. *J. Clim.* **22**, 615–632 (2009).
38. Kug, J.-S., Jin, F.-F. & An, S.-I. Two Types of El Niño Events: Cold Tongue El Niño and Warm Pool El Niño. *J. Clim.* **22**, 1499–1515 (2009).
39. Yeh, S.-W. et al. El Niño in a changing climate. *Nature* **461**, 511–514 (2009).
40. Song, G. & Ren, R. C. Linking the Subsurface Indian Ocean Dipole to Central Pacific ENSO. *Geophys. Res. Lett.* **49**, e2021GL096263 (2022).
41. Huang, B. et al. Extended Reconstructed Sea Surface Temperature, Version 5 (ERSSTv5): Upgrades, Validations, and Intercomparisons. *J. Clim.* **30**, 8179–8205 (2017).
42. Rayner, N. A. et al. Global analyses of sea surface temperature, sea ice, and night marine air temperature since the late nineteenth century. *J. Geophys. Res.: Atmospheres* **108**, 4407 (2003).
43. Ishii, M., Shouji, A., Sugimoto, S. & Matsumoto, T. Objective analyses of sea-surface temperature and marine meteorological variables for the 20th century using ICOADS and the Kobe Collection. *Int. J. Climatol.* **25**, 865–879 (2005).
44. Reynolds, R. W., Rayner, N. A., Smith, T. M., Stokes, D. C. & Wang, W. An Improved In Situ and Satellite SST Analysis for Climate. *J. Clim.* **15**, 1609–1625 (2002).
45. Zuo, H., Balmaseda, M. A., Tietsche, S., Mogensen, K. & Mayer, M. The ECMWF operational ensemble reanalysis–analysis system for ocean and sea ice: a description of the system and assessment. *Ocean Sci.* **15**, 779–808 (2019).
46. Carton, J. A. & Giese, B. S. A Reanalysis of Ocean Climate Using Simple Ocean Data Assimilation (SODA). *Mon. Weather Rev.* **136**, 2999–3017 (2008).
47. Behringer, D. et al. Evaluation of the global ocean data assimilation system at NCEP: The Pacific Ocean. 11–15 (2004).
48. Köhl, A. Evaluating the GECCO3 1948–2018 ocean synthesis – a configuration for initializing the MPI-ESM climate model. *Q. J. R. Meteorol. Soc.* **146**, 2250–2273 (2020).
49. Kalnay, E. et al. The NCEP/NCAR 40-Year Reanalysis Project. *Bull. Am. Meteorol. Soc.* **77**, 437–472 (1996).
50. Allan, R. & Ansell, T. A New Globally Complete Monthly Historical Gridded Mean Sea Level Pressure Dataset (HadSLP2): 1850–2004. *J. Clim.* **19**, 5816–5842 (2006).
51. Zhao, S., Jin, F.-F. & Stuecker, M. F. Improved Predictability of the Indian Ocean Dipole Using Seasonally Modulated ENSO Forcing Forecasts. *Geophys Res Lett.* **46**, 9980–9990 (2019).
52. Zhao, S. et al. Improved Predictability of the Indian Ocean Dipole Using a Stochastic Dynamical Model Compared to the North American Multimodel Ensemble Forecast. *Weather Forecast* **35**, 379–399 (2020).

Acknowledgements

This work was supported by the National Research Foundation of Korea grants funded by the Korean government (NRF-2018R1A5A1024958, RS-2023-00208000, NRF-2023R1A2C1004083). S.I.A. was supported by the Yonsei Fellowship, funded by Lee Youn Jae and Yonsei Signature Research Cluster Program (2021-22-0003). SOEST # 11825 and IPRC # 1622.

Author contributions

H.-J.P. and S.-I.A. initiated and led the study. H.-J.P. performed the analyses and developed the analytical methods. J.-H.P., M.F.S., C.L. and S.-W.Y. participated in discussions, and all authors contributed to the writing of the manuscript.

Competing interests

The authors declare no competing interests.

Additional information

Supplementary information The online version contains supplementary material available at https://doi.org/10.1038/s43247-024-01525-1.

Correspondence and requests for materials should be addressed to Soon-Il An.

Peer review information *Communications Earth & Environment* thanks the anonymous reviewers for their contribution to the peer review of this work. Primary Handling Editors: Min-Hui Lo, Heike Langenberg. A peer review file is available.

Reprints and permissions information is available at http://www.nature.com/reprints

Publisher's note Springer Nature remains neutral with regard to jurisdictional claims in published maps and institutional affiliations.

Open Access This article is licensed under a Creative Commons Attribution 4.0 International License, which permits use, sharing, adaptation, distribution and reproduction in any medium or format, as long as you give appropriate credit to the original author(s) and the source, provide a link to the Creative Commons licence, and indicate if changes were made. The images or other third party material in this article are included in the article's Creative Commons licence, unless indicated otherwise in a credit line to the material. If material is not included in the article's Creative Commons licence and your intended use is not permitted by statutory regulation or exceeds the permitted use, you will need to obtain permission directly from the copyright holder. To view a copy of this licence, visit http://creativecommons.org/licenses/by/4.0/.

© The Author(s) 2024